### Global Bifurcations in Rayleigh-Bénard Convection: Experiments, Empirical Maps and Numerical Bifurcation Analysis

I. G. Kevrekidis and R. Rico-Martínez
Department of Chemical Engineering, Princeton University,
Princeton, NJ 08544-5263

R. E. Ecke<sup>1</sup>, R. M. Farber<sup>2</sup> and A. S. Lapedes<sup>2</sup>

<sup>1</sup>Physics Division and Center for Nonlinear Studies

<sup>2</sup>Theoretical Division

Los Alamos National Laboratory, Los Alamos, NM 87545

October 24, 2018

#### Abstract

We use nonlinear signal processing techniques, based on artificial neural networks, to construct an empirical mapping from experimental Rayleigh-Bénard convection data in the quasiperiodic regime. The data, in the form of a one-parameter sequence of Poincaré sections in the interior of a mode-locked region (resonance horn), are indicative of a complicated interplay of local and globalbifurcations with respect to the experimentally varied Rayleigh number. The dynamic phenomena apparent in the data include period doublings, complex intermittent behavior, secondary Hopf bifurcations, and chaotic dynamics. We use the fitted map to reconstruct the experimental dynamics and to explore the associated local and global bifurcation structures in phase space. Using numerical bifurcation techniques we locate the stable and

unstable periodic solutions, calculate eigenvalues, approximate invariant manifolds of saddle type solutions and identify bifurcation points. This approach constitutes a promising data post-processing procedure for investigating phase space and parameter space of real experimental systems; it allows us to infer phase space structures which the experiments can only probe with limited measurement precision and only at a discrete number of operating parameter settings.

### 1 Introduction

When presented with experimental observations of the dynamics of a nonlinear system at a discrete number of operating parameter settings, it is often difficult to interpret the global phase space structure underlying the experimental time series, or to get a good picture of the state of the system at intermediate parameter values. It would therefore be desirable to develop a model of the experimental dynamics that could be implemented, simulated and analyzed on the computer. Several approaches are possible: one could start from the fundamental equations for the system, impose realistic boundary conditions, and simulate the resulting set of equations. For experiments described by partial differential equations, such an approach is often untenable, requiring extensive computational resources. Even though necessary for the fundamental understanding of the instabilities underlying the dynamics, this approach may not quantitatively reproduce the finer details of the observed behavior. This may be because of small deviations from the idealizations of the model, imperfections of the apparatus, oversimplified boundary conditions, imperfect estimation of physical properties, inaccurate readings of the experimental settings, etc. The second approach, which more practically aims at interpreting the particular experimental observations, is to fit the observed dynamics with a dynamical system (a map, or a set of ODEs) of the appropriate phase space dimension. As we shall see, this approach is capable, at least for the experimental data we have considered, of reproducing significant features of the dynamics and yielding insight into the properties of the phase-space structure underlying the observed behavior. Techniques for the reconstruction of phase-space mappings have been developed for dynamical systems analysis [11, 21] and recently for the purpose of prediction and forecasting of time series (see for example [4] and references therein). These methods include functional approximation using radial basis functions, local-linear maps, and neural network algorithms.

In this paper we use the latter approach (i.e., fitting the observed dynamics) incorporating in the model a functional dependence on a bifurcation parameter; this can easily be generalized to multiple parameters. This type of empirical modeling provides crucial assistance in conjunction with numerical bifurcation analysis [3, 24] for interpreting the bifurcation structures "contained in" (or consistent with) the experimental data. More generally, such techniques can play a significant role in real-time prediction and control

applications for a large class of physical systems (see for example the recent experimental literature on stabilizing unstable periodic orbits [25, 26]). They can be thought of as a useful data compression and post-processing tool, which assists the concise presentation and interpretation of experimental time series.

In this work we consider the dynamics of data from a Rayleigh-Bénard convection experiment in a region of parameter space where the behavior is complicated and difficult to interpret by visual inspection of the Poincaré section data alone. The paper is organized as follows: the next section is a description of the experiment and of the experimental data. We then outline briefly the data processing technique used (Artificial Neural Networks, ANNs) and discuss its performance in fitting the data. Using the fitted map(s) we construct a plausible picture of the bifurcation structures in phase and parameter space using numerical bifurcation methods. Finally, we discuss the applicability of this approach to a wider class of problems.

### 2 Experimental Data

The experimental data presented here are obtained from a rectangular small-aspect-ratio convection cell used for studies of low-dimensional nonlinear dynamics. The convecting fluid is a 1.46 % solution of <sup>3</sup>He in superfluid <sup>4</sup>He and thermal convection is induced by applying a fixed heating current to the top plate while maintaining the bottom plate at fixed temperature. Details of the experimental apparatus and properties of the superfluid mixture are described elsewhere [8, 19]. Here we discuss the measurement probe and present a brief characterization of the parameter space of thermal convection in this system.

For a fixed geometry, two dimensionless parameters characterize the convective state. The Rayleigh number R, proportional to the temperature difference across the fluid layer  $\Delta T$ , is a measure of the driving force applied to the system. The other dimensionless parameter in the problem is the Prandtl number  $\sigma$ , which measures the ratio of the rates of molecular diffusion of momentum and heat and controls details of the secondary instabilities in thermal convection. In  ${}^{3}\text{He}{}^{-4}\text{He}$  mixtures  $\sigma$  is a strong function of the mean temperature  $T_{m}$  of the cell, and is varied over the quasiperiodic regime in the range  $0.06 < \sigma < 0.08$  by varying the mean temperature in the

Figure 1: Convective dynamic states in two-parameter (Rayleigh number and Prandtl number) space. Dynamic behavior in the various regions is described in the text.

range  $0.83 < T_m < 0.90$ K.

For small R, the fluid conducts heat diffusively. At  $R \approx 2000$  there is a forward (supercritical) bifurcation to steady convection [19] where the fluid motion is believed to be two convection rolls oriented parallel to the short side of the rectangular convection cell. At higher values of R the flow becomes time dependent, going through a sequence of bifurcations from periodic to quasiperiodic to chaotic dynamics. The state of the time-dependent convective flow is partially determined from measurements of the spatially-averaged convective heat transport. In small-aspect-ratio convection, however, the side walls severely constrain the spatial structure of the fluid flow, and measurement of the dynamics of the system at a single point is often adequate to characterize the dynamical nature of the state. Therefore, in addition to a global measure of the temperature field from the time dependence of the top-bottom temperature difference, we use a thermal probe which measures a local temperature difference near the center of the cell top plate with a temperature sensitivity of  $0.3 \times 10^{-7} \text{K/Hz}^{1/2}$  [19]. We denote the measured temperature difference at the local probe by  $\delta T(t)$ . The output of this probe is digitized to produce a time series record of the system dynamics.

In order to understand the context of the data, we now describe briefly

the relevant regions of parameter space, see Fig. 1. The first time dependent solution "begins" at the transition to periodic oscillations of frequency  $f_1$  (typically  $f_1 \approx 0.6$  Hz). This transition is a forward Hopf bifurcation in R [8], and its critical R value depends strongly on  $\sigma$ . Another Hopf bifurcation at higher R gives rise to a second frequency  $f_2$ , incommensurate with the first. This second mode is only weakly interacting with the initial limit cycle mode and not until there is a discontinuous transition to a different second mode does measurable mode-locking occur. Within a region of parameter space above the discontinuous transition, quasiperiodic (incommensurate frequencies), mode-locked and chaotic states exist [9, 10, 13].

Fig. 2 shows the various data processing stages of a "typical" experimental run, in this case for  $R/R_c = 12.01$ ,  $1/\sigma = 14.97$ . (a) shows a segment of the experimental time series; (b) shows the corresponding power spectrum (calculated from the time series using an FFT algorithm with standard windowing techniques), marking the frequencies  $f_1$  and  $f_2$  from fitting. Standard techniques of phase space reconstruction [11, 21] are used to produce phase space trajectories of the dynamical system; (c) shows a projection of the continuous attractor reconstructed with two time delays,  $\tau_1 = 2s$  and  $\tau_2 = 1s$ (the phase space for all the attractors in this paper has been normalized so that the limits of the attractors are  $\pm 1$ ); and finally (d) shows the Poincaré section obtained from this attractor by transversely intersecting it with a plane defined by x(t) = -0.15 and only plotting intersections in a single direction. How this particular section arises will be discussed later. The location and orientation of the Poincaré plane is variable, so that we can choose sections with the minimum of overlappings and projection singularities usually arising in delay coordinate reconstructions of dynamical attractors. Using these techniques we can characterize the evolution of dynamical states of the system as R is varied.

The dynamics in the quasiperiodic regime are often "summarized" in terms of a single number, the winding or rotation number  $W \equiv f_2/f_1$ , where  $f_1$  and  $f_2$  are the fundamental frequencies (practically determined from spectral analysis of the time series data). The mode-locking structure known as the "devil's staircase" is constructed from a sequence of such spectra as a function of  $R/R_c$  at fixed  $\sigma$ . Such a representative structure is illustrated in Fig. 3, obtained from experimental data (the Rayleigh number is normalized with the critical  $R_c = 2000$ ). By making a series of such measurements at different values of  $\sigma$ , the locking regions in the  $\{R/R_c, \sigma\}$  parameter space

Figure 2: The various data processing stages of the experimental run: (a) a segment of the experimental time series, (b) the power spectrum, (c) a projection of the reconstructed attractor using time delays (notice the location of the plane (x(t) = -0.15) used to generate the Poincaré section shown in (d)).

are determined, Fig. 4. These regions, called "Arnol'd horns" or "resonance" horns, are seen to broaden as  $\sigma$  decreases (this is why we plot  $1/\sigma$  in the ordinate in Fig. 4) indicating that the coupling or nonlinearity of the oscillatory modes varies roughly with  $1/\sigma$ . Similarly the value of the winding number is controlled primarily by changing  $R/R_c$ .

For  $1/\sigma < 14$ , the dynamics of the system are well described by the circle map model [7, 10, 13]. For special irrational winding numbers, the universality predicted for the attractor has been verified in this system [10, 20]. Somewhat higher up in the horns more complicated behavior appears, arising via global bifurcations [9, 15]. It is this region of parameter space that concerns us here. In Fig. 5 we illustrate the detailed structure in the neighborhood of the W=2/13 locking. Significant features in addition to quasiperiodic and mode-locked regions include secondary Hopf bifurcations of the mode-locked periodic orbit, period doubling bifurcations, regions of complicated transient behavior, and apparently chaotic states whose appearance is probably associated with the occurrence of global bifurcations. Hysteresis in the transitions between these states can be thought of as indicative of such global bifurcations, as computational and theoretical work on many model systems shows. Fig. 6 is a representative experimental plot of the hysteretic behavior of the winding number for ascending and descending sequences of  $R/R_c$  [15]. The effective winding number of the Poincaré sections,  $\rho$ , is related to W measured from the power spectra by  $\rho = 1/W$ , mod 1. So for W=2/13 we get  $\rho = 1/2$  which gives a period-2 cycle with two points in the Poincaré section [7, 13]. Our purpose in the next sections is to describe the complicated dynamics represented by these data with a simple empirical mapping as a function of a single control parameter,  $R/R_c$ . We will use fitting techniques to generate such an input-output map that can be analyzed with numerical bifurcation methods.

### 3 Empirical Map Construction

We used a standard ANN configuration [17] to process the time series from the experimental results sampled in Fig. 7. The experimental information is in the form of a (nonlinear) map F:

$$\mathbf{X_n} \overset{\mathbf{F}(\mathbf{X},R)}{\longrightarrow} \mathbf{X_{n+1}}$$

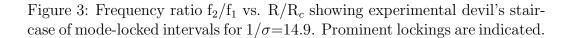


Figure 4: Experimental regions of mode locking in the  $1/\sigma$  and  $R/R_c$  parameter space. The dashed lines represent the hysteretic discontinuity at low  $R/R_c$ , increasing  $R/R_c$  (- - - - -) and decreasing (- - - -), and a transition to high dimensional chaos at large  $R/R_c$ . For  $1/\sigma > 15$  there is structure in the horns not shown on this global plot.

Figure 5: Fine structure of the 2/13 resonance horn. Secondary Hopf bifurcations (S.H.B.), period doublings, hysteresis, intermittency and resonance horn overlaps are shown.

where  $\mathbf{X} = [x \ y]^T$  are the coordinates of the intersections of the trajectory with the Poincaré plane,  $\mathbf{X_n}$  and  $\mathbf{X_{n+1}}$  are two such successive intersections, and R is the value of the operating parameter, the Rayleigh number.

While a first visual inspection of the phase portraits in Fig. 7 might indicate that a map of the plane would constitute a satisfactory representation of the data, a more careful study reveals that there exist folds in the projection used (see for example Fig. 7H or Fig. 7L). We were not able to find a two-dimensional plane that would "get rid of" these projection singularities for *all* the phase portraits involved in this one-parameter cut. For that reason, and in order to obtain a deterministic map, we used one more delay in the reconstruction of the attractor. This means that we chose to fit a (four-dimensional) map  $\mathbf{F}$  of the form  $\mathbf{X_{n+1}} = \mathbf{F}(\mathbf{X_n}, \mathbf{X_{n-1}}, R)$ .

Artificial neural networks (see Fig. 8) are structures composed of many interconnected processing units (neurons). A fully connected network distributes the outputs of every neuron in a given layer to all the neurons of the layer above. The input layer is composed of "fan-out" units whose function is only to distribute their inputs to the neurons in the next layer.

Figure 6: W vs R/R<sub>c</sub> for ascending (+) and descending ( $\circ$ ) sequences (1/ $\sigma$  = 14.97). Prominent lockings are labeled.

The neurons of the intermediate or "hidden" layers compute as their output a scalar nonlinear function (usually of sigmoidal shape) of a weighted sum of their inputs. The input to one of the neurons of the first hidden layer is the sum  $\sum_i a_i X_i + b$ ;  $X_i$  are the outputs of the layer below (the input layer), and the constants  $a_i$  and b (which are different for each neuron and are called "weights" and "offsets", respectively) will be determined, as we discuss below, by "training" the network. The outputs of the neurons of this first hidden layer will then serve as inputs of the neurons of the second hidden layer, with new weights and offsets, and so on. The neurons of the output (final) layer simply produce linear functions (linear combinations plus a scalar offset) of their inputs.

These structures have been found to have universal approximator properties: they can be used to construct approximations (outputs) of continuous functions of n real variables (inputs) with support in the unit hypercube [5, 14]. The standard ANN architecture used in this work consists of a four layered network: input layer, output layer and two hidden layers. This

Figure 7: A sampling of the experimental Poincaré sections used for training the ANN. The experimental observations depicted in the "upper" sequence (O through L) are indicative of a large amplitude invariant circle while the ones in the "lower" sequence (A through J) are related to the period-2 resonant solution. The contiguous sequence A through J was broken in the figure only because of space limitations. The overlap zone demonstrates the observed bistability (hysteresis). The parameter values  $(R/R_c)$  are as follows A: 12.057, B: 12.040, C: 12.032, D: 12.019, E: 12.0150, F: 12.011, G: 12.007, H: 12.002, I: 11.986, J: 11.982, K: 11.987, L: 11.983, M: 11.979, N: 11.950 and O: 11.946.

Figure 8: Schematic representation of the ANN configuration used. All layers are fully interconnected; a few of the connections are depicted.

particular structure has been found to be, in practice, successful in the identification of nonlinear mappings based on time series data (e.g. [17]).

The feedforward artificial neural networks we used had an input layer consisting of four neurons for the system state and one neuron for the operating parameter. The output layer consisted of two neurons that predict the point at which the continuous time trajectory will next intersect the plane which defines the Poincaré section. In order to successively iterate the ANN, both outputs have to be fed back into the corresponding inputs (schematically depicted in Fig. 8 with dash—dot lines).

The weights and offsets of the ANN that provide the "best" approximation (outputs) of the observed measurements as a function of previous measurements (inputs) are determined by "training" the network: a least squares minimization problem. The objective function is the norm of the difference between ANN predictions and actual experimental measurements of the states after one iteration of the Poincaré map. Training was performed

using a conjugate gradient algorithm, with the map and derivative evaluations performed in parallel using a SIMD computer (the 64,000 processor CM-200) at the Advanced Computing Laboratory at LANL. The implementation we used is therefore ideally suited to very large sets (many thousands) of data points.

In the process of this research we trained several ANNs, all of them containing two hidden layers; the "best" results presented here were obtained with 10 nonlinear neurons per hidden layer, each neuron with activation function  $g(X) = \frac{1}{2}(1 + tanh(X))$ , in addition to the input and output layers whose neurons are linear (see Fig. 8). As there is currently no rigorous way to determine an optimum number of neurons for a particular set of data, the number of neurons in the hidden layers is somewhat arbitrary (see for example [16]). Our choice here reflects a compromise between the computational effort required to train the ANN and an estimate of the minimum number of neurons needed to capture the underlying dynamics.

The training set from each "experimental run" contains about 300 Poincaré section points; an "experimental run" consists of time series measurements obtained at a single value of the operating parameter, and is considered to be converged on the attractor, in the sense that measurements during an initial period following the parameter change (transient data approaching the attractor) are not used in the training. In principle, it would be desirable to include such transient data in the training, since this would provide information about the dynamics "away" from the attractor in phase space, and would also provide to the ANN quantitative information about the rate of approach to the attractor (and thus its stability characteristics).

A total of 55 different experimental runs were available for this value of the Prandtl number,  $1/\sigma=15.04$  (27 from experiments obtained with *increasing* R, and the remaining obtained with *decreasing* R). Appendix A (Figures 22 and 23) at the end of the paper shows the entire set of experimental observations used for training. For this comparatively small data set a CM-200 is not necessary to successfully train a network in a realistic amount of time. However, as the complexity and the dimensionality of the behavior grow, along with the size of the data set, our parallel implementation should become indispensable.

### 4 Interpretation of the data

In what follows, we will present our *a priori* "best guess" of a consistent sequence of bifurcations underlying the phase portraits in Fig. 7 as illustrated in the schematic bifurcation diagram of Fig. 9. While some of our interpretations may appear somewhat arbitrary at first, a reader experienced in the study of resonance phenomena for maps or periodically-forced oscillators will find such bifurcation sequences in the quasiperiodic regime quite familiar.

Our data start at  $R/R_c=12.052$ , roughly in the middle of the 2/13 resonance horn; we clearly see a period-2 attractor, phase portrait A in Fig. 7. We will call this the "resonant" period-2; it is associated with the 2/13 resonance horn, and the boundaries of the horn correspond to saddle-node bifurcations involving this period-2 solution. At higher values of the Prandtl number (lower down the horn in Figs. 4 and 5) the data clearly indicate that this saddle-node bifurcation occurs on a smooth invariant circle, Fig. 10 [15]. One therefore expects a saddle period-2 to coexist with the stable period-2, and a "minimal" requirement of the fitted map would be to predict the existence of such a solution. The fitted map should also exhibit a saddle-node bifurcation involving this saddle and the resonant period-2 at low values of R, i.e. at the boundary of the resonance horn.

A supercritical (soft) Hopf bifurcation occurs with decreasing R, giving rise to a small amplitude period-2 invariant circle (phase portrait B). The model should be capable of predicting this Hopf bifurcation, i.e., the stable period-2 solution should lose stability with two eigenvalues of its linearization exiting the unit circle in the complex plane. Furthermore, the model should predict an unstable (source) period-2 solution surrounded by the period-2 stable invariant circle.

The period-2 invariant circles grow in amplitude and deform (phase portraits C and D), and the first "nontrivial" transition occurs between phase portraits D (showing a period-2 "cuspy" invariant circle) and phase portrait E, showing a period-16 stable solution. The period-16 points are obviously located close to the eight "cusps" or corners developed by the period-2 circles. It is in principle possible that these apparent cusps may be the result of a singularity due to the projection to a two-dimensional picture. Because of the intensely deformed nature of the circles, however, we do not believe that this period 16 is the result of frequency-locking on the circles. We suggest that a saddle-node of period-8 solutions occurs away from the period-2

Figure 9: Tentative schematic bifurcation diagram of the transitions observed in the experimental data. Solid lines indicate stable periodic solutions, broken lines indicate unstable solutions and filled circles indicate period-2 small amplitude invariant circles (small) or large amplitude invariant circles (large).

Figure 10: A sequence of Poincaré sections obtained at  $1/\sigma = 14.749$ , lower down the 2/13 resonance horn. They clearly indicate the birth of a stable (resonant) period-2 in a saddle-node bifurcation on the invariant circle.

circles. The period-2 circles, growing in amplitude, are then lost via a global bifurcation involving their interaction with the saddle period-8 solution (this is consistent with the pronounced cusps developing on the invariant circles). The stable period-8 solution then undergoes a cascade of period doublings, resulting first in the observed period-16 (phase portrait E) and eventually in an 8-horseshoe-piece apparently chaotic attractor (phase portrait F). This attractor then undergoes a reverse sequence of period doublings, coming back to a period 16 (phase portrait G), a period 8, and finally resulting in phase portrait H.

Fig. 9 summarizes our interpretation of these transitions: the stable period-2 undergoes a "soft" Hopf bifurcation, and the resulting stable period-2 invariant circle grows and is eventually destroyed in a global bifurcation involving the stable and unstable manifolds of the saddle-type period-8 solutions. These period-8 solutions exist on an isola: a saddle-node pair of period-8 solutions is born and eventually disappears in saddle-node period-8 bifurcations. The stable node period-8 becomes a focus, then an inverse node, and finally undergoes a period-doubling cascade, followed by a reverse cascade, and disappearing in the "other" saddle-node end of the isola. Notice that our interpretation predicts a small hysteresis interval where stable period-8 solutions coexist with a stable period-2 invariant circle. It is in principle possible to avoid this by assuming that the period-8 solution results from frequency locking on the period-2 invariant circles; it is the "pointed" nature of the shape of the circles that argues against such an interpretation.

It is tempting to consider that the reverse sequence of these bifurcations occurs as the bifurcation parameter R is further reduced: A global bifurcation involving the saddle period-8 stable and unstable manifolds "gives rise" again to large amplitude period-2 invariant circles (slightly wrinkled) in phase portrait H. The amplitude of the circles diminishes (phase portraits I and J), but here the analogy with the high R behavior stops: there is no evidence of a low-R Hopf bifurcation, nor is there a stable period-2 observed in the data. Instead, the behavior "jumps" directly from large amplitude period-2 invariant circles to a large amplitude attractor. Indeed, this large amplitude attractor coexists with the large amplitude period-2 invariant circle (that is the hysteresis observed at the edge of the resonance horn in Fig. 6). The large amplitude attractor gradually develops into a smooth large amplitude invariant circle in phase portrait N, and shows clearly a saddle-node period-5 frequency locking between phase portraits N and O. That this latter bifurca-

tion is indeed a saddle-node bifurcation on the invariant circle is supported by the accumulation of experimental points on the large invariant circle in phase portrait N, occurring at five distinct locations. The stable period-5 should be accompanied by a saddle period-5, and has rotation number  $f_2/f_1 = 5/33$ . This would then imply that frequency lockings predicted by the Farey sequence should exist (and the largest ones could be detected) between the 5/33 and the 2/13 resonances: there is experimental evidence of the 12/79 and 7/46 lockings in the data.

The large amplitude invariant circle (denoted by large filled circles in Fig. 9) develops a number of frequency lockings (indicated by the "flat" parts of its evolution in the bifurcation diagram), reminiscent of the truly flat intervals of frequency locking in a rotation number vs. R plot.

Based on this information, here is a plausible explanation of what occurs as R grows from lower to higher values: At some point an "invisible" saddle-node (saddle-source) bifurcation of period-2 solutions occurs, away in phase space from the large amplitude invariant circle. A global bifurcation, involving the saddle-type period-2 solutions gives rise to finite-amplitude period-2 invariant circles, thus leading to an interval of hysteresis between the stable period-2 invariant circles and the large amplitude attractor; this is the hysteresis observed experimentally close to the boundary of the horn. In this case of multistability, the basin boundary between the two attractors (the large-amplitude invariant circle and the period-2 invariant circles) is provided by the stable manifolds of the saddle-type period-2 solutions. Finally, these same saddle period-2s are responsible for the end of the hysteresis interval: the large amplitude invariant circle approaches these two saddle points, and is lost in a global bifurcation involving their stable and unstable manifolds.

This interpretation is "realistic" in that it involves only generic codimension-1 bifurcations, which are furthermore known to occur in similar regimes for maps of the plane (see for example [1, 12, 23].) The only "unusual" element is that the saddle-node bifurcation at the boundary of the resonance horn is now a saddle-source; both period-2 solutions born there are unstable. This interpretation is due to the fact that no stable period-2 points were observed for low R in the one-parameter diagram. We saw that "lower down" the resonance horn (lower  $1/\sigma$ ) this saddle-node bifurcation yields a stable node (Fig. 10); this would then imply the existence (in a two-parameter continuation) of a Takens-Bogdanov point [2, 27] (two eigenvalues of the resonant period-2 solution at 1) on the boundary of the resonance horn some-

where in the vicinity of our experimental one-parameter cut. Since secondary Hopf bifurcation curves emanate from such codimension-2 bifurcation points [23, 12, 22], this interpretation is also corroborated by the existence of period-2 invariant circles nearby, and the observation of secondary Hopf bifurcations along the experimental one-parameter cut. A plausible embedding of this one-parameter cut in a two-parameter diagram is presented and discussed in Section 6.

This inferred sequence of bifurcations is consistent with the observed phase portraits. The important question is whether a model based on – and consistent with – the experimental data will indeed exhibit these bifurcations at intermediate values of the control parameter (R).

## 5 The ANN based models and their predictions

As we discussed in section 3, we chose to train an ANN with five neurons in the input layer, two in the output layer and two-hidden layers with 10 neurons each. The training set consisted of data obtained at ascending (Fig. 22) and descending (Fig. 23) values of R; the entire set of available data was used. The training was successful, in that the resulting map was capable of accurately predicting the one-step-ahead data it was fitted to. More importantly, when this map was iterated indefinitely, the qualitative nature and quantitative location of its attractors was comparable to the experimental ones. We will start investigating and comparing the numerically predicted and experimentally observed (actually inferred) bifurcations from the interior of the horn  $R/R_c \approx 12.049$  towards its left boundary with decreasing values of  $R/R_c$ . Figure 11 shows a sequence of qualitative transitions between experimental phase portraits (top row) and predicted long-term attractors (bottom row). A bifurcation diagram constructed using the model is also shown in Fig. 11: the stable period-2 indeed undergoes a Hopf bifurcation at  $R/R_c = 12.0257$ (the experimental value is somewhat higher, at  $R/R_c \approx 12.046$ ). Stable and unstable solutions have been calculated through Newton iteration and standard continuation techniques. Local bifurcations were found using standard numerical bifurcation algorithms (e.g. the package AUTO by Prof. E. Doedel [6]). The model does predict the supercritical "soft" nature of the

Figure 11: Comparison of experimental (top row) versus predicted (bottom row) attractors, and partial bifurcation diagram predicted by the first ANN trained. The parameter values  $(R/R_c)$  for the portraits are as follows: A: 12.0196, B: 12.033, C: 12.041, D: 12.050. A' and D' same as A and D, B': 12.0200, C': 12.023.

bifurcation. The amplitude of the period-2 invariant circles grows, and they develop sharp "corners" as do the experimental attractors.

A saddle-node of period-8 solutions is observed at  $R/R_c = 12.0210$ , and the model predicts a short interval of hysteresis (coexistence of the stable period-8 and stable period-2 invariant circles). The period-2 invariant circles are lost after a global bifurcation involving the stable and unstable manifolds of the saddle-period 8 solutions. This bifurcation is illustrated in Fig. 12. The figure shows (enlarged in the vicinity of one of the two period-2 invariant circles) the situation before (panel A) and after the bifurcation (panel B). In panel A both sides of the one-dimensional unstable manifold of the saddles period-8 are eventually attracted by period-8 nodes (no hysteresis). In panel B one side of the unstable manifold approaches the period-8 nodes, while the other side spirals inward and asymptotically approaches the stable period-2 invariant circle. The change in the structure of the unstable manifolds of the saddle period-8 solutions indicates the nature of the bifurcation: a homoclinic crossing between the stable and unstable manifolds of the saddle period-8. In this case the unstable manifold is one-dimensional, while the stable manifold is three-dimensional (since we are using a map in  $\mathbb{R}^4$ ). This global bifurcation does not occur at a single parameter value, but over an interval in parameter space (starting with a homoclinic tangency, followed by crossing and ending again by a tangency between the stable and unstable manifolds of the saddle). This interval is extremely narrow here (almost impossible to computationally resolve in double precision) and for all practical purposes this transition occurs at  $R/R_c \approx 12.01948$ .

The qualitative success of the fitted map in reproducing the bifurcations of the period-8 solutions, however, stops here. The period-8 solutions do not period-double (for the model) to a period-16 and above, nor is there a reverse cascade; they persist until  $R/R_c=12.0136$ , when they disappear in a saddle-node bifurcation with the saddle period-8s (compared with the experimentally interpolated value of  $R/R_c\approx 12.006$ ). The ANN was somewhat –but not completely– successful in "learning" these bifurcations: it can reproduce a part of the transitions required to get to the period-doubling, but it does not "go all the way" (the eigenvalues do not get to cross -1). This shortcoming may be at least in part attributed to the fact that there is a comparatively small amount of experimental (training) data in this regime, and that no transient data were available; nevertheless, as we will discuss below, there is a "quick fix" for this problem.

Figure 12: Phase portraits before and after the global bifurcation associated with the disappearance of the period-2 invariant circles as predicted by the first ANN trained. The parameter values  $(R/R_c)$  are A: 12.0193 and B: 12.0196. • indicates saddles and o indicates nodes. Notice the difference in the relative location of the saddle unstable manifolds in the two pictures.

This initial ANN is significantly more successful in capturing the low-R bifurcation patterns (see Fig. 13): a "reverse" global bifurcation, involving again the stable and unstable manifolds of the saddle-period 8 solutions gives rise to two finite-amplitude invariant circles at  $R/R_c \approx 12.0151$ . After the period 8 solutions have disappeared in a saddle-node bifurcation, closing the period-8 isola, the only visible attractor left is these finite-amplitude period 2 invariant circles. Of course, the ANN predicts both period-2 periodic solutions: the saddle, and the source whose projection is located "inside" the two invariant circles <sup>1</sup>. This is clearly seen in Fig. 13G. As the Rayleigh number is decreased, the finite-amplitude period-2 invariant circles continue to exist (Fig. 13F and E) but the ANN correctly predicts hysteresis between them and a large amplitude attractor (Fig. 13P). The appearance of this attractor is associated with a global bifurcation involving the saddle period-2 solutions. This can be seen in Fig. 13P by the proximity of the attractor

<sup>&</sup>lt;sup>1</sup> Since the map is 4-dimensional, the "source" is really a *saddle*: it has two stable eigenvalues in the full space, and two unstable ones. We call it a "source" because of the analogy with resonances and Hopf bifurcations in maps of the plane.

Figure 13: Representative phase portraits predicted by the first ANN trained (low  $R/R_c$ ). The parameter values ( $R/R_c$ ) of the model for the portraits are as follows: A: 11.9430, B: 11:9513, C:11.9541, D: 11.9653, E: 11.9848, F: 11.9876, G: 11.9898, H: 11.9374, I:11.9485, J:11.9530, K: 11.9653, L: 11:9745, M: 11.9775, N: 11.9792, O: 11.9876 and P: 11.9898.

and the saddle period-2 solutions. Detailed calculations show that in the hysteretic regime, one side of the (one-dimensional) unstable manifold of the saddle period-2 solutions asymptotically approaches the finite amplitude period-2 invariant cirles, while the other side asymptotically approaches the large amplitude attractor. At the high-R "boundary" of the hysteresis a homoclinic interaction occurs between the unstable and stable manifolds of the period-2 solutions. The quotation marks indicate that this transition does not occur at a single parameter value, but through the onset and end of a homoclinic tangle. This tangle would appear "heteroclinic" for the second iterate of the Poincaré map: the stable manifold of each of the period-2 points interacts with the unstable manifold of the "other" period-2 point.

Returning to the "upper" solution branch, as the Rayleigh number is decreased through the hysteresis regime (towards Fig. 13E), the finite amplitude period-2 invariant circles approach the period-2 saddles, and finally disappear. Their destruction involves another global bifurcation: another homoclinic interaction of the stable and unstable manifolds of the saddle period-2 points. The difference is that now the "other" sides of the one-dimensional unstable manifolds are involved, and the bifurcation would also appear as homoclinic for the *second* iterate of the map. The two boundaries of hysteresis constitute, therefore, two different global bifurcations involving the saddle period-2 invariant manifolds.

Phase portraits 13E and 13N also illustrate the need for embedding in a space with more than two dimensions: in the projection used, one of the two period-2 invariant circles falls "inside" and the other one "outside" the coexisting large amplitude attractor. This would not be possible for a *uniquely invertible* map of the plane.

As the Rayleigh number is further decreased (Fig. 13N through H) the large amplitude attractor continues to exist; it deforms as the parameter changes, and develops a number of frequency lockings, the most prominent of which is the period-5 solution visible in Fig. 13I (compare also with the experimental data in Fig. 7).

The ANN is therefore capable of qualitatively capturing all the phase portraits observed experimentally. In addition, now that we can calculate the saddle-type solutions and study numerically their unstable manifolds, we have confirmed the nature of the global bifurcations we proposed in the previous section as marking the boundaries of the hysteresis between the finite-amplitude period-2 invariant circles and the large amplitude attractor.

Figure 14: Bifurcation diagram computed using the first ANN trained. Solid lines indicate stable periodic solutions, broken lines indicate unstable solutions and filled circles indicate period-2 small amplitude invariant circles (small) or large amplitude invariant circles (large). Notice the hysteresis around  $R/R_c \approx 11.99$  and the isolated solutions around  $R/R_c \approx 11.95$ .

Figure 15: Representative phase portraits predicted by the second ANN trained (high  $R/R_c$ ). The parameter values ( $R/R_c$ ) of the model for the portraits are as follows: A: 11:9942, B: 12:0015, C: 12.0135, D: 12.0140, E: 12.0149, F: 12.0179, G: 12.0213, H: 12.0218, I: 12.0223 and J: 12.0433.

No further hysteresis was observed in this regime during the experimental runs, for either ascending or descending Rayleigh numbers. The last element of our postulated bifurcation diagram to be confirmed was the saddle-node (saddle-source) bifurcation marking the end of the 2/13 resonance horn. As can be seen, however, in Fig. 13D through A, the ANN predicts a new region of hysteresis (actually an isolated region). A saddle-stable node bifurcation is predicted at  $R/R_c = 11.9386$ , giving rise to a stable period-2 attractor (Fig. 13A). This attractor coexists with the large amplitude one (Fig. 13I, J) and the basin boundary consists of the stable manifolds of the saddle type period-2 solutions formed in the same saddle-node bifurcation (the "resonant" saddle period-2 as we have been referring to it). As R is increased, a Hopf bifurcation occurs at  $R/R_c = 11.9484$  giving rise to two small amplitude period-2 invariant circles. These grow in amplitude, and are lost in one more global bifurcation(s) involving the saddle period-2 stable and unstable manifolds, leaving the large-amplitude attractor as the only stable solution. The nature of this global bifurcation is again obvious from Fig. 13C and D from the relative location of the period-2 stable invariant circles and the resonant period-2 saddles. The low-R predictions of this ANN are summarized in the computed bifurcation diagram of Fig. 14, which illustrates the hysteretic regime observed experimentally (period-2 invariant circles with large amplitude attractor), as well as the yet unconfirmed lower-R multistability region predicted by the ANN.

Since this additional multistability region is isolated, it is quite natural that it was not observed with the experimental procedure followed. The ANN therefore predicts a bifurcation sequence equally plausible (and equally compatible with the data) as the one we initially guessed and illustrated schematically in Fig. 9. While it confirms a number of our "guesses" on the bifurcations underlying the transitions between different phase portraits, it also poses a new experimental question: how could we confirm or rule out the predicted low-R multistability region? In experimental terms, how could we systematically try to obtain data on this isolated solution branch? This is precisely the type of feedback we expect from a data post-processing procedure, and we will further discuss below the design of experiments motivated from this prediction.

We now return to the single inconsistency between this ANN and the experimental data: while it essentially matched every experimental observation, the network did not predict the forward and reverse cascade of period-

Figure 16: Bifurcation diagram computed using the second ANN trained. Solid lines indicate stable periodic solutions, broken lines indicate unstable solutions and filled circles indicate period-2 small amplitude invariant circles.

Figure 17: Blowup of the previous bifurcation diagram in the neighborhood of the period-8 isola. Notice the pair of period doublings bifurcations to period-16 solutions. A forward and a reverse cascade of period doublings (not shown in detail) occur around  $R/R_c \approx 12.02$ .

doublings of the period-8 solutions to apparent chaos. As we discussed above, this should be at least partly attributed to the comparatively small number of data available in this regime, and the lack of transient information. To rectify this, we gave more weight to the high-R experimental data in the overall training set (to be exact, we considered the data of panels Q, R, S and T in Fig. 22 and panels J, K and L in Fig. 23 twice in the training set). We then expect this "second" ANN to more accurately capture the dynamics at higher values of R; this is indeed the case, as can be seen in both the computed phase portraits of Fig. 15 and the corresponding computed bifurcation diagram of Fig. 16.

Consider the sequence of representative phase portraits predicted by the second ANN (Fig. 15A through J). At high values of R (Fig. 15J) we find

the stable period-2 resonant solution, which as in the case of the first ANNundergoes a Hopf bifurcation to a small-amplitude period-2 invariant circle (Fig. 15I). The sequence of bifurcations starts here exactly as was discussed above for the first ANN: a saddle-node period-8 bifurcation, giving a stable and a saddle period-8 (Fig. 15H) (along with a small interval of hysteresis, too narrow to be observed experimentally); then loss of the small amplitude invariant circle in a global bifurcation involving the stable and unstable manifolds of the saddle period-8 solutions. But now the sequence changes, and the second ANN does indeed reproduce the experimental bifurcations: a period-doubling of the period-8 to a period-16 solution  $(R/R_c = 12.0223,$ see Fig. 15G) and a subsequent cascade of period doublings resulting in an 8-horseshoe segment apparently chaotic attractor (Fig. 15F). This is followed by a reverse cascade of period doublings ending up with a period 16 (Fig. 15E) and a period-8 (Fig. 15D) exactly as the experimental data show. The period-8 isola closes in a saddle-node bifurcation  $(R/R_c = 12.0085)$  just after two finite-amplitude "invariant circles" are formed by a homoclinic interaction of the saddle period-8 solutions (jump to the attractor in Fig. 15C after a very narrow hysteresis interval). These finite-amplitude period-2 invariant circles continue to deform smoothly as R decreases further, and eventually are lost around  $R/R_c = 11.9940$ . As we discussed in detail above, this is due to a global bifurcation (a homoclinic interaction) involving the stable and unstable manifolds of the resonant saddle period-2 solutions. This is again indicated in Fig. 15A by the proximity of the projections of the two invariant circles with the resonant period-2 saddles predicted by this network. Exactly as we discussed above, this bifurcation causes a "jump" to the coexisting large amplitude attractor. The sequence is summarized in the computed bifurcation diagram of Fig. 16, which –along with its blowup in Fig. 17– should be compared with the schematic diagram we postulated in Fig. 9. The qualitative agreement was excellent for lower values of R and partially successful in the high-R regime with the first ANN; with the second ANN the agreement now extends over the entire region of available experimental data.

### 6 Discussion

We found that the use of ANNs to study our experimental data from the quasiperiodic regime of Rayleigh-Bénard convection constitutes a valuable post-processing tool. The deterministic maps fitted to Poincaré sections of the experimental time-series measurements were, as a rule, accurate in reproducing the short term system dynamics. They were also quite successful in predicting the long-term attractors, and providing the sequence of bifurcations leading from one to the other.

The one-parameter bifurcation diagram found using the ANN (summarized schematically in Fig. 18) is consistent with the data; it guides –through confirmation or by providing a possible alternative—our interpretation of the phase portraits and our guesses of the transitions between them as the Rayleigh number varies. It also guides our experimental search of critical parameter values, by interpolating or extrapolating from the available data. One particularly interesting feature of the bifurcation diagram predicted by the ANN is a multistability regime which was not observed experimentally. This regime, however, could not be observed experimentally the way the experimental procedure was performed, since the "additional" attractors were isolated. This example provides an indication of how the ANN can guide a subsequent experimental search: if a two-parameter diagram is constructed (by training the ANN using data from additional one-parameter cuts at different Rayleigh numbers) we can draw a good guess of a path in two-parameter space that could take us smoothly to the isolated attractors. This path (as can be deduced from the two-parameter picture postulated below) would involve sequences of experiments at higher Prandtl numbers, when the isolated attractor branch "connects" with the attractors we did trace experimentally.

A significant stumbling block in this work was the determination of the dimension of the embedding space. While all the phenomena predicted by the network could in principle occur in maps of the plane, we could not locate a simple two-dimensional Poincaré section of the data that would give plausible phase portraits. The fact, for example, that one of the two small period-2 invariant circles seems to fall "inside" the coexisting large amplitude invariant circle in Fig. 13P, while the second period-2 invariant circle seems to fall "outside", is an indication that folds exist in this projection. We had to use a higher number of delays in order to obtain such a picture with a deterministic invertible map. In principle there is no problem with a higher dimensional

Figure 18: Schematic one parameter bifurcation diagram, showing a summary of the ANN predictions. Solid lines indicate stable periodic solutions, broken lines indicate unstable solutions and filled circles indicate period-2 small amplitude invariant circles (small) or large amplitude invariant circles (large).

Figure 19: Schematic two parameter bifurcation diagram, showing the 2/13 resonance horn in the neighborhood of the experimental data. The nature of the one-parameter bifurcation curves can be inferred from the short description in Table 1. The middle one-parameter cut corresponds to the one actually predicted by the second ANN, while the upper is the one we postulated upon inspection of the experimental phase portraits. The lower one-parameter cut is the one identified by the first ANN trained.

Figure 20: Schematic phase portraits representative of the correspondingly numbered regions of the postulated two-parameter bifurcation diagram (Fig.19).

Figure 21: Schematic phase portraits (a) and blowups (b) representative of the regions numbered 7 and 11 in the postulated two-parameter bifurcation diagram (Fig.19). Notice the hysteresis between invariant circle period-2 solutions and period-8 fixed points, and the difference in the relative arrangement of the coexisting attractors and the period-8 saddle invariant manifolds.

map (the embedding dimension based on Takens' version of Whitney's theorem should be higher than two), but working in a four-dimensional space prevents us from visualizing the stable manifolds of the saddle resonant solutions, which now are three-dimensional hypersurfaces in four-space. Had we been able to find a convenient projection that would allow us to fit a map of the plane, it would have been possible to numerically approximate the stable manifolds of the saddle-type solutions too. The procedure used here should in principle be applicable to data and attractors of higher dimensions; it is, however, important for the success of the process that extensive data are available not only on the attractor – and, for that matter, distributed over the entire attractor in phase space –, but also on transients approaching it. In such cases the number of data points used in training would grow significantly, and then the massively parallel algorithm we used would be truly valuable. For the case studied here (approximately 15000 data points) it is still possible to train the ANN on a powerful workstation.

Another point worth making is the invertibility of the fitted map (i.e. that every point should possess a unique preiterate, or, in other words, trajectories on the attractor do not cross forward or backward in time). This is a fundamental property of Poincaré maps obtained from sets of ODEs, and hence it is a natural constraint on the process. In principle, however, neural network maps (like polynomial or rational polynomial maps) are not necessarily uniquely invertible; there may exist regions of phase space for which several preimages of a given phase point are possible. This should not be thought of as an insurmountable problem: a little thought (and a study of the 1989 paper by E. Lorenz [18]) will show that every simple explicit integration scheme can be noninvertible! In our case, the requirement is that the ANN should remain uniquely invertible in the relevant regions of phase space: those corresponding to realistic initial conditions, and especially in regions containing training data. The phase portraits predicted by the ANN will be consistent with those predicted by deterministic and uniquely invertible maps as long as initial conditions in the "relevant" region have a single preimage –or, if they have more than one, only one falls in the "relevant" region while all the additional spurious ones are far away (in phase space) from the experimental data. This invertibility problem can also be avoided if we perform an identification of a continuous time system (a set of ODEs) as opposed to a discrete map [24]; but then the geometric simplification of the Poincaré section is lost.

With some weighting of the data in one regime of initial discrepancy, we have now (a) a complete qualitative -and reasonable quantitative- consistency between the experimental and the predicted data, (b) a confirmation of the local and global bifurcations underlying the observed transitions and hysteresis regimes, and (c) a guide to further design of experiments.

Fig. 19 is a plausible schematic two-parameter bifurcation diagram, including what would correspond to both Rayleigh and Prandtl number changes. While in this paper we quantitatively studied data along a single one-parameter cut, detailed two parameter experimental data as well as extensive studies of model systems in the quasiperiodic regime lead us to draw the interior of the 2/13 resonance horn as shown. Table 1 summarizes the various bifurcations in Fig. 19 in a compact form, while Fig. 20 and Fig. 21 provides a quick schematic reference of the qualitative phase portraits expected in each region.

The sides of the resonance horn are saddle-node bifurcation curves of period-2 solutions. A secondary Hopf bifurcation curve arises at a postulated Takens-Bogdanov point on the left hand side of the resonance horn. This is a point at which two eigenvalues of the Poincaré map are equal to 1, and one expects both a secondary Hopf bifurcation curve (a Hopf of the resonant period-2 solutions to period-2 invariant circles) as well as a global bifurcation involving these invariant circles and the saddle resonant period-2 solutions, in the neighborhood of such a point. A "downward" dip of the secondary Hopf curve is consistent with experimental data at lower values of  $1/\sigma$  ([20, 9]). A different homoclinic global bifurcation, associated with the hysteresis between the resonant period-2 and the large amplitude attractor, "starts" lower down on the left-hand-side of the resonance horn. This type of bifurcation is discussed in detail in [1, 9]. The secondary Hopf bifurcation has its own resonance horns, one of which (the one giving rise to a period-8 solution) is shown schematically in Fig. 19. This resonance horn –higher up in it—contains the successive nested period-doubling curves, as well as -at its sides—the narrow hysteresis regions with the coexistence of the period-8 solutions and the small amplitude period-2 invariant circles.

The sequence of bifurcations observed in the experimental one-parameter cut can be succintly followed with the help of Table 1. If a one-parameter cut is taken schematically just a little higher in  $1/\sigma$ , we obtain the bifurcation diagram postulated initially in Section 4. If, on the other hand, a one-parameter cut is taken schematically just a little lower in  $1/\sigma$ , we obtain

the bifurcation diagram predicted by the first ANN trained: the one where all transitions except the period doubling cascades of the period-8 solution were captured. It is well known that two parameters are necessary to map the quasiperiodic regime (at least close to a Hopf bifurcation). Even though our one-parameter dependent ANN was qualitatively quite successful, this discussion clearly indicates that two-parameter data are required in order to construct a complete picture of the bifurcations of the system. This is a direction we are currently pursuing.

### 7 Acknowledgements

This work was partially supported by DARPA/ONR grant N00014-91-J-1850 (IK, RR, AL, RF), the Exxon Education Foundation (IK,RR), and by the U.S. Department of Energy, Office of Basic Energy Science, Division of Materials Science (RE). IK also gratefully acknowledges a David and Lucile Packard Foundation Fellowship.

# A Experimental portraits used during the training of the ANNs.

Figs. 22 and 23 show all the experimental data used during the training of the ANNs.

### References

- [1] D. G. Aronson, M. A. Chory, G. R. Hall and R. P. McGehee, Bifurcations from an invariant circle for two-parameter families of maps of the plane: a computer-assisted study, *Commun. Math. Phys.*, **83**:303 (1988).
- [2] R. I. Bogdanov, Versal Deformation of a Singular Point on the Plane in the Case of Zero Eigenvalues, *Func. Anal. Appl.* **9**:144 (1975).
- [3] P. Bryant and C. Jeffries, The Dynamics of Phase Locking and points of Resonance in a Forced Magnetic Oscillator, *Physica* **25D**:196 (1987).
- [4] M. Casdagli, S. Eubank, J.D. Farmer, and J. Gibson, State Space Reconstruction in the Presence of Noise, *Physica* **51D**:52 (1991).
- [5] G. Cybenko, Approximation by Superposition of a Sigmoidal Function, *Math. Control Signals Systems* **2**:303 (1989).
- [6] E.J. Doedel, and J.P. Kernévez, AUTO: A Program for Continuation and Bifurcation Problems in Ordinary Differential Equations, Applied Mathematics Report, *California Institute of Technology* (1986).
- [7] R.E. Ecke, Quasiperiodicity, Mode-Locking, and Universal Scaling in Rayleigh-Bénard Convection, in 'Chaos, Order, and Patterns,' ed. by R. Artuso, P. Cvitanovic, and G. Casati (Plenum Press, NY, 1991), p. 77.
- [8] R.E. Ecke, H. Haucke, Y. Maeno and J.C. Wheatley, Critical Dynamics at a Hopf Bifurcation to Oscillatory Rayleigh-Bénard Convection, *Phys. Rev.* A 33:1870 (1986).
- [9] R.E. Ecke and I.G. Kevrekidis, Interactions of Resonances and Global Bifurcations in Rayleigh-Bénard Convection, *Phys. Lett.* A 131:344 (1988).

- [10] R.E. Ecke, R. Mainieri, and T.S. Sullivan, Universality in Quasiperiodic Rayleigh-Bénard Convection, *Phys. Rev.* A 44:8103 (1991).
- [11] A. Fraser and H.L. Swinney, Independent Coordinates for Strange Attractors from Mutual Information, *Phys. Rev.* A 33:1134 (1986).
- [12] J.M. Gambaudo, Perturbation of Hopf Bifurcation by an External Time-Periodic Forcing, J. Diff. Equ. 57:172 (1985).
- [13] H. Haucke and R.E. Ecke, Mode Locking and Chaos in Rayleigh-Bénard Convection, *Physica* **25D**:307 (1987).
- [14] K. Hornik, M. Stinchcombe, and H. White, Multilayer Feedforward Networks are Universal Approximators, *Neural Networks* **2**:359 (1989).
- [15] I.G. Kevrekidis and R.E. Ecke, Global Bifurcations in Maps of the Plane and in Rayleigh-Bénard Convection, *Cont. Math.* **99**:313 (1989).
- [16] M.A Kramer, and J.A. Leonard, Diagnosis Using Backpropagation Neural Networks-Analysis and Criticism, *Computers chem. Engng.* **14**:1323 (1990).
- [17] A.S. Lapedes and R. Farber, Nonlinear Signal Processing using Neural Networks: Prediction and System Modeling, Los Alamos Report LA-UR 87-2662, (1987).
- [18] E.N. Lorenz, Computational Chaos A Prelude to Computational Instability, *Physica* **35D**:299 (1989).
- [19] Y. Maeno, H. Haucke, R.E. Ecke, and J.C. Wheatley, Oscillatory Convection in a Dilute <sup>3</sup>He-Superfluid-<sup>4</sup>He Solution, *J. Low Temp. Phys.* **59**:305 (1985).
- [20] R. Mainieri, T.S. Sullivan, and R.E. Ecke, Two-Parameter Study of the Quasiperiodic Route to Chaos in Convecting <sup>3</sup>He-Superfluid-<sup>4</sup>He Mixtures, *Phys. Rev. Lett.* **63**:2357 (1989).
- [21] N.H. Packard, J.P. Crutchfield, J.D. Farmer, and R.S. Shaw, Geometry from a Time Series, *Phys. Rev. Lett.* **45**:712 (1980).

- [22] S. Pavlou and I.G. Kevrekidis., Microbial Predation in a Periodically Operated Chemostat: a Global Study of the Interaction between Natural and Externally Imposed Frequencies, *Math. Biosci.* **108**:1 (1992).
- [23] B.B. Peckham, The Closing of Resonance Horns for Periodically Forced Oscillators, PhD thesis, University of Minnesota (1988).
- [24] R. Rico-Martínez, K. Krischer, I. G. Kevrekidis, M. C. Kube and J. L. Hudson, Discrete- vs. Continuous-Time Nonlinear Signal Processing of Cu Electrodissolution Data, Chem. Eng. Comm., 118:25 (1992).
- [25] I. B. Schwartz and I. Triandaf, Tracking Unstable Orbits in Experiments, *Phys. Rev. A* **46**:7439 (1992).
- [26] T. Shinbrot, W. Ditto, C. Grebogi, E. Ott, M. Spano and J. A. Yorke, Using the Sensitive Dependence of Chaos (the "Butterfly Effect") to Direct Trajectories in an Experimental Chaotic System, *Phys. Rev. Lett.* 68:2863 (1985).
- [27] F. Takens, Singularities of Vector Fields, *Publ. Math.* **IHES 43**:47 (1974).

Figure 22: Experimental Poincaré sections, used for training of the ANN; the data in this figure were obtained starting at low  $R/R_c$ , and increasing with constant step. The parameter values  $(R/R_c)$  are as follows A: 11.941, B: 11.946, C: 11.950, D: 11.954, E: 11.958, F: 11.962, G: 11.966, H: 11.970, I: 11.975, J: 11.979, K: 11.983, L: 11.987, M: 11.991, N: 11.995, O: 12.000, P: 12.004, Q: 12.008, R: 12.012, S: 12.016, T: 12.020, U: 12.025, V: 12.029, W: 12.030, X: 12.037 Y: 12.041, Z: 12.046 and A<sub>2</sub>: 12.050.

Figure 23: Experimental Poincaré sections, used for training of the ANN; the data in this figure were obtained starting at high  $R/R_c$ , and decreasing with constant step. The parameter values  $(R/R_c)$  are as follows A: 12.053, B: 12.048, C: 12.044, D: 12.040, E: 12.036, F: 12.032, G: 12.028, H: 12.023, I: 12.019, J: 12.015, K: 12.011, L: 12.007, M: 12.003, N: 11.998, O: 11.994, P: 11.990, Q: 11.986, R: 11.982, S: 11.977, T: 11.973, U: 11.969, V: 11.965, W: 11.961, X: 11.957, Y: 11.952, Z: 11.948, A<sub>2</sub>: 11.944 and B<sub>2</sub>: 11.940.

TABLE 1	
Transition Boundary	Description of transition
1-2	Saddle-node (sink) bifurcation of the period-2 solution
1-4	Saddle-node (source) bifurcation of the period-2 solution
2-3	Hopf bifurcation of the period-2 solution
2-5	Global bifurcation, homoclinic tangle of the manifolds
	of the saddle period-2; associated with the formation
	(or destruction) of a stable large amplitude invariant circle
3-4	Global bifurcation, homoclinic tangle of the manifolds
	of the saddle period-2; associated with the formation
	(or destruction) of a stable period-2 invariant circle
3-6	Global bifurcation, homoclinic tangle of the manifolds
	of the saddle period-2; associated with the formation
	(or destruction) of a stable large amplitude invariant circle
5-6	Hopf bifurcation of the period-2 solution
5-12	Hopf bifurcation of the period-2 solution
5-13	Saddle-node bifurcation of the period-2 solution
6-7	Saddle-node bifurcation of the period-8 solution
6-8	Saddle-node bifurcation of the period-8 solution
7-8	Global bifurcation, homoclinic tangle of the manifolds
	of the saddle period-8; associated with the formation
	(or destruction) of a stable period-2 invariant circle
8-9	Period doubling bifurcation of the period-8 solution
8-11	Global bifurcation, homoclinic tangle of the manifolds
	of the saddle period-8; associated with the formation
	(or destruction) of a stable period-2 invariant circle
8-12	Saddle-node bifurcation of the period-8 solution
9-10	Subsequent period doubling bifurcations
11-12	Saddle-node bifurcation of the period-8 solution

Table 1: Transitions associated with the two-parameter bifurcation diagram.